The Mechanism of Charge Generation in Charge-Generation Units Composed of p-Doped Hole-Transporting Layer/HATCN/n-Doped Electron-Transporting Layers

*Sunghun Lee, Jeong-Hwan Lee, Jae-Hyun Lee, and Jang-Joo Kim**

The rate-limiting step of charge generation in charge-generation units (CGUs) composed of a p-doped hole-transporting layer (p-HTL), 1,4,5,8,9,11-hexaazatriphenylene hexacarbonitrile (HATCN) and n-doped electron-transporting layer (n-ETL), where 1,1-bis-(4-bis(4-methyl-phenyl)-amino-phenyl)-cyclohexane (TAPC) was used as the HTL is reported. Energy level alignment determined by the capacitance–voltage (*C–V*) measurements and the current density–voltage characteristics of the structure clearly show that the electron injection at the HATCN/n-ETL junction limits the charge generation in the CGUs rather than charge generation itself at the p-HTL/HATCN junction. Consequently, the CGUs with 30 mol% Rb_2CO_3-doped 4,7-diphenyl-1,10-phenanthroline (BPhen) formed with the HATCN layer generates charges very efficiently and the excess voltage required to generate the current density of ±10 mA cm^{-2} is around 0.17 V, which is extremely small compared with the literature values reported to date.

1. Introduction

Organic light-emitting diodes (OLEDs) are actively being research for solid-state lighting and flexible displays as well as for large size displays. Solid-state lighting requires a high luminance of more than a few thousands candela m^{-2}. Since OLEDs are current-driven devices, high luminance requires there to be high current into the device, resulting in the reduction of the device's operational lifetime. High current efficiency and long operational lifetimes could be achieved by using a tandem structure, which reduces the current density into the OLED at high luminance.[1,2]

Tandem OLEDs are accomplished by vertically stacking a few emitting units in series, where each emitting unit consists of a hole-transporting layer (HTL)/emitting layer (EML)/electron-transporting layer (ETL) structure. The emitting units are interconnected by charge-generation units (CGUs). A major challenge in tandem OLEDs is to develop a high-performance CGU between individual emitting units, which requires efficient charge generation with small extra voltage drops as well as optical transparency.[2–14] Among various types of CGUs, HTL/metal oxide or an organic hole-injection layer (HIL) with a deep-lying lowest unoccupied molecular orbital (DL-LUMO) energy level/n-doped organic ETL junction are promising for efficient charge generation.[3–7,10–14] Transition metal oxides such as V_2O_5, WO_3, MoO_3, and ReO_3 and organic materials such as 1,4,5,8,9,11-hexaazatriphenylene hexacarbonitrile (HATCN) have been used as materials with DL-LUMO energy levels, resulting in reduced driving voltages, improved voltage stability, prolonged lifetimes, and improved power efficiencies.[4–6] Among them, HATCN has the advantage of low-temperature deposition, which is compatible with the fabrication process for OLEDs.

Although the characteristics of tandem OLEDs using HATCN as a component of the CGU have been reported,[5,6] few studies have been devoted to providing detailed information about how the performance of charge generation is related to its constituent materials.

In this study, we investigated the factors influencing charge generation in the CGU composed of p-HTL/HATCN/n-ETL. In particular, we focused on the effect of the n-doped ETL of the CGU by using different ETLs, while using 1,1-bis-(4-bis(4-methyl-phenyl)-amino-phenyl)-cyclohexane (TAPC) as the HTL. Three different ETLs of 4,7-diphenyl-1,10-phenanthroline (BPhen), bis-4,6-(3,5-di-3-pyridylphenyl)-2-methylpyrimi-dine (B3PYMPM), and 2,2′,2″-(1,3,5-benzenetriyl)tris-[1-phenyl-1H-benzimidazole] (TPBi) were selected for this purpose. Energy level alignment determined by capacitance–voltage (*C–V*) measurements and current density–voltage (*J–V*) characteristics of the structure clearly showed that electron injection at the HATCN/n-ETL junction and electron transport in the n-ETL limit the charge generation in the CGUs rather than charge generation itself at the p-HTL/HATCN junction.

2. Results and Discussion

The chemical structures of the materials used in this work are shown in **Figure 1**. The energy levels were determined by

S. Lee, J.-H. Lee, J.-H. Lee, Prof. J.-J. Kim
WCU Hybrid Materials Program
Department of Materials Science and Engineering
and the Center for Organic Light Emitting Diode
Seoul National University
Seoul, 151-744, Korea
E-mail: jjkim@snu.ac.kr

S. Lee
OLED Research Institute
Samsung Mobile Display Co., LTD.
Giheung-Gu, Yongin-City, 446-711, Korea

DOI: 10.1002/adfm.201102212

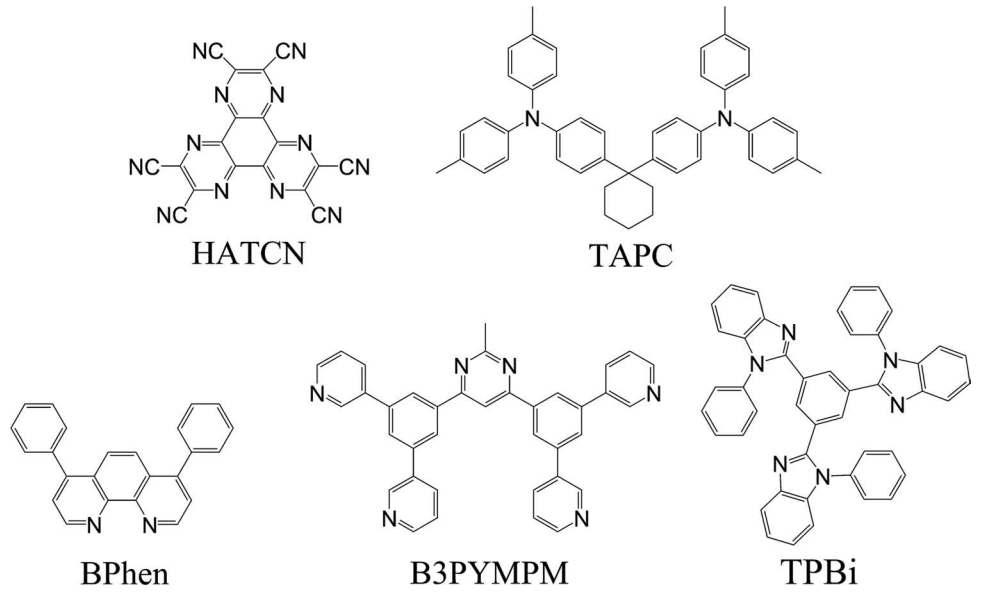

Figure 1. Structures of the molecules studied in this paper: HATCN, TAPC, BPhen, B3PYMPM, and TPBi.

ultraviolet photoemission spectroscopy (UPS) and UV–vis absorption spectroscopy;[15,16] the electron mobilities, measured using the time of flight method,[17–20] of HATCN and the ETL materials are summarized in **Table 1**. In order to understand the charge generation process of the CGUs composed of p-HTL/HATCN/n-ETL, we prepared devices consisting of indium tin oxide (ITO)/8 wt% ReO_3-doped TAPC (30 nm)/HATCN (20 nm)/n-doped ETLs (20 nm)/15 wt% Rb_2CO_3-doped B3PYMPM (30 nm)/Al (100 nm). BPhen, B3PYMPM, and TPBi were selected as the ETLs in order to investigate their effects on the performance of the charge generation. Rb_2CO_3 was used as the n-dopant with a 30 mol% concentration in the devices. The 30 nm thick 8 wt% ReO_3-doped TAPC and 15 wt% Rb_2CO_3-doped B3PYMPM layers were used to reduce the resistance for the charge transport and to remove the energy barrier for the charge injection to the adjacent electrodes from the CGUs. **Figure 2**a shows the *J–V* characteristics of the CGUs with different ETLs. The devices with B3PYMPM and TPBi CGUs show asymmetric *J–V* characteristics in the forward and reverse biases. However, the device with BPhen shows a much higher current density than the B3PYMPM- and TPBi-based CGUs and a symmetric *J–V* characteristic in the forward and reverse biases, indicating that the charge generation is much more efficient in the BPhen-based CGU than the other CGUs. We can divide the charge-generation process of the CGU with p-HTL/HATCN/n-ETL into two steps: the charge generation at the p-HTL/HATCN junction and the electron and hole injection and transport to the neighboring layers. Significant differences in the *J–V* characteristics of the devices with different n-ETLs clearly indicate that the rate-limiting step in the charge generation process of the CGUs is the charge injection at the HATCN/n-ETL junction and transport in the n-ETL, rather than the charge generation itself at the HATCN/p-HTL junction. The voltage required for –10 mA cm^{-2} in the reverse bias is only –0.56 V in the BPhen-based CGU, while those for the B3PYMPM- and TPBi-based CGUs are –2.9 and –3.1 V, respectively. The trend is the same in the forward bias; the voltage required to get 10 mA cm^{-2} is only 0.39 V for the BPhen CGU, while those for the B3PYMPM and TPBi CGUs are 1.35 and 1.88 V, respectively. The differences between the forward and reverse absolute voltages at ±10 mA cm^{-2}, representing an asymmetry factor in the *J–V* characteristics, are 0.17, 1.19, and 1.55 V for BPhen, TPBi, and B3PYMPM, respectively. Moreover, the BPhen device showed space-charge-limited current (SCLC) behavior represented by $J \approx V^2$ (Figure 2b), indicating that the current is limited by transport through the organic layers with small injection barriers at the HATCN/n-BPhen and n-BPhen/n-B3PYMPM junctions. In contrast, the currents of the other devices are limited by the junction characteristics.

Table 1. Energy levels of the electronic structure and electron mobilities of HATCN, BPhen, B3PYMPM, and TPBi.

ETLs	HATCN	BPhen	B3PYMPM	TPBi
HOMO [eV]	–9.9[15]	–6.0[16]	–6.75[16]	–6.15[16]
LUMO [eV]	–6.0[15]	–2.6[16]	–3.15[16]	–2.65[16]
Optical band gap [eV]	3.9[15]	3.4[16]	3.6[16]	3.5[16]
Electron mobility [$cm^2\ V^{-1}\ s^{-1}$][a)]	$\approx 10^{-4}$[20]	5.2×10^{-4}[17]	1.5×10^{-5}[18]	5×10^{-5}[19]

[a)]All electron mobilities from the references were measured using the time of flight method.

In order to understand the differences among the ETLs, we performed the *C–V* measurements and determined the electronic structures of the CGUs. The *C–V* characteristics of the three devices are shown in **Figure 3**. The capacitance of the device with the BPhen based CGU is ≈3 to 5 times larger than the other devices at zero bias and drops rapidly at voltages above 0.1 V to reach to less than 5 nF at 1 V in the forward direction. Since the capacitance is related to the depletion region in the CGU, the large capacitance implies that the depletion width

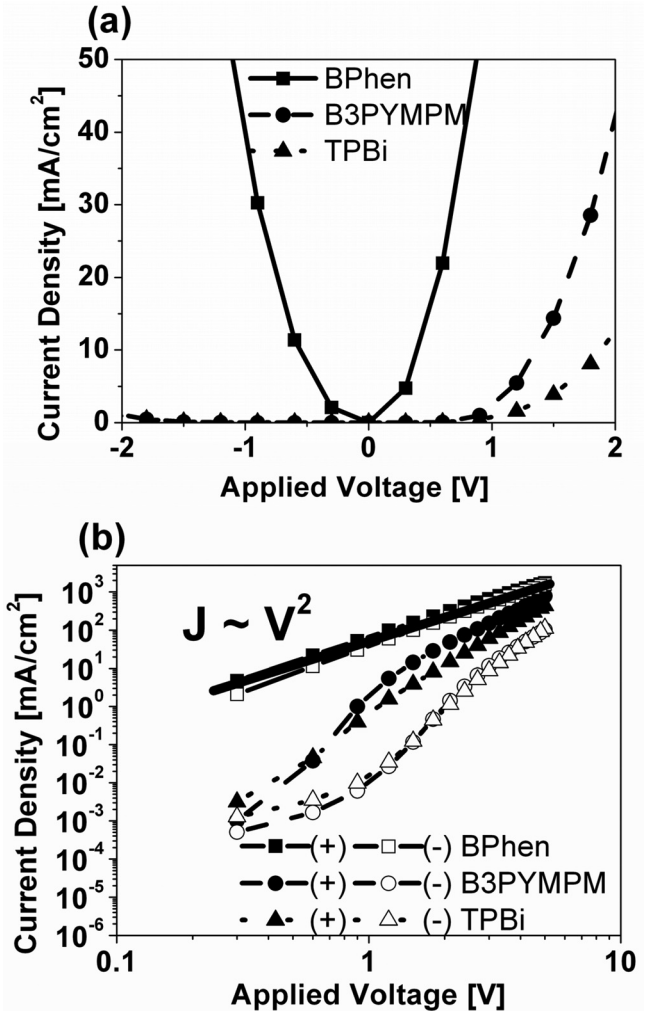

Figure 2. a) Linear *J–V* characteristics for different electron transporting layers. b) Log–log *J–V* characteristics for different ETLs of samples with glass substrate/patterned ITO (150nm)/TAPC-ReO_3 (8 wt%, 30 nm)/HATCN (20 nm)/ETLs-Rb_2CO_3 (30 mol%, 20 nm)/B3PYMPM-Rb_2CO_3 (15 wt%, 30 nm)/Al (100 nm). Current density is the absolute value, the filled symbols hold for the forward bias direction, the open symbols hold for the reverse bias direction. The solid line is added as a guide for the eye, illustrating a slope of 2, which is the dependence expected for the space charge limited current.

in the junction at $V = 0$ is very narrow. The rapid decrease in the capacitance above 0.1 V indicates that the injected charge carriers from both electrodes begin to recombine in the CGU at 0.1 V, probably through tunneling, and that the tunneling probability increases rapidly with increasing voltage to lose the charge storage capacity in the junction. The low voltage of 0.1 V required for the tunneling suggests that there are negligible voltage drops in the other layers in the CGU.

In contrast to the BPhen device, the devices with the B3PYMPM- and TPBi-based CGUs show much lower capacitances than the BPhen-based device, suggesting that the depletion width is much wider than it is in the BPhen-based device. The capacitance increases a little up to 1 V followed by a gradual decrease with a further increase of applied voltage. This behavior can be understood by the narrowing of the depletion

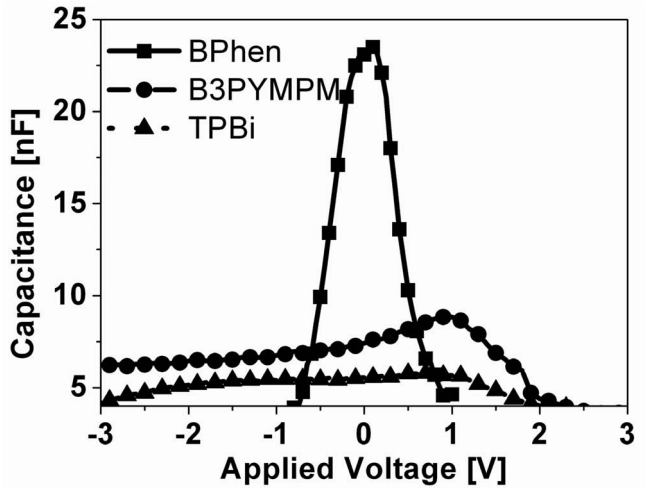

Figure 3. *C–V* characteristics for different electron transporting layers (measured at 1 kHz and with an applied ac bias voltage of 10 mV) of samples with glass substrate/patterned ITO (150nm)/TAPC-ReO_3 (8 wt%, 30 nm)/HATCN (20 nm)/ETLs-Rb_2CO_3 (30 mol%, 20 nm)/B3PYMPM-Rb_2CO_3 (15 wt%, 30 nm)/Al (100 nm).

layer up to 1 V and the fact that the electrons are starting to be injected from n-B3PYMPM and n-TPBi to the HATCN and they are then recombined with the injected holes at the p-TAPC/HATCN junction above 1 V, where the transition voltage of 1 V can be interpreted as the built-in potential in the n-ETL layer.[21] This interpretation is supported by the coincidence between the onset voltages in the *J–V* curves in the forward bias, which are 0.9 and 1.06 V at 1 mA cm^{-2}, and the transition voltages in the *C–V* curves, with values around 1 V for B3PYMPM- and TPBi-based CGUs, respectively. In contrast to the B3PYMPM and TPBi, it is difficult to estimate the built-in potential in the n-doped BPhen layer from the *C–V* curve because the rapid drop of the capacitance at 0.1 V is not coming from the reduction of the barrier with increasing forward bias, but rather from the occurrence of electron tunneling through the junction even though the forward bias has not reached the built-in potential of the n-BPhen junction.The capacitance of the BPhen-based device in the reverse bias also reduced rapidly with increasing voltage. In contrast, the capacitances of the devices with B3PYMPM and TPBi CGUs show small decreases with applied reverse bias. For simple consideration, we have assumed that the electrode/doped organic junctions and n-ETLs/n-B3PYMPM junctions are Ohmic contacts and the resistance of the bulk organic layer is much smaller than the HATCN/n-ETL junction. These assumptions have been shown to be valid in the cases of the doped organic layers and the HATCN layer.[15,22] The devices can then be simplified as planar capacitors of the HATCN/n-ETL junctions, which correspond to n–n heterojunctions. Under these assumptions, the rapid reduction of the capacitance in the BPhen-based CGU under reverse bias indicates that charges generated at the p-HTL/HATCN junction can easily tunnel through the HATCN/n-BPhen junction even at the very low voltage of –0.1 V. In contrast, a small decrease of capacitance combined with a low current in the B3PYMPM- and TPBi-based devices imply the widening of the depletion region in the HATCN/n-B3PYMPM and HATCN/n-TPBi junctions.

The n-layer with a higher work function is accumulated by the majority carrier, the electron, in the n–n heterojunction and the built-in potential by band bending resulting from this accumulation is very small compared to that of the other n-layer with a lower work function by depletion. Therefore, the capacitance of the n–n heterojunction is approximately assumed to be due to metal–semiconductor contact.[23] Under the assumption, the depletion widths (W) in n-ETLs at 0 V estimated from the known capacitances of the devices using Equation (1) are 5.4, 16.7 and 22.3 nm for BPhen, B3PYMPM, and TPBi, respectively.

$$W = \varepsilon_r \varepsilon_0 \frac{A}{C_0} \tag{1}$$

where ε_r is the relative dielectric constant of the n-ETL, ε_0 is the permittivity of free space, C_0 is the capacitance at 0 V, and A is the area of the cell. A relative dielectric constant of 3.5 was used for the organic materials.[26]

The calculated depletion widths and the built-in potential in the HATCN/n-ETL junction at 0 V allow us to calculate the free carrier density in the n-ETLs using the Mott–Schottky equation[24,25]

$$n = \frac{2\varepsilon_r \varepsilon_0 \psi}{q W^2} \tag{2}$$

where q is the electric charge and ψ is the built-in potential in the n-ETLs. With 1 V built-in potentials in B3PYMPM- and TPBi-based CGUs, the estimated carrier densities of the 30 mol% Rb_2CO_3-doped B3PYMPM and TPBi layers were 1.4×10^{18} and 0.78×10^{18} cm^{-3}, respectively. The estimated carrier densities are very close to the values of 2×10^{18} and 0.7×10^{18} cm^{-3} for B3PYMPM and TPBi, respectively, as measured from the ITO/LiF (50 nm)/n-ETL/Al (metal/insulator/doped semiconductor/metal) structures using the Mott–Schottky equation.[16] As described before, it is difficult to estimate the built-in potential in BPhen from the C–V data. Instead, using the carrier density of 6.0×10^{18} cm^{-3} for the n-doped BPhen from a published reference[16] and the estimated width of the depletion layer of 5.4 nm from our C–V data, we can estimate the built-in potential of Rb_2CO_3-doped BPhen side, using Equation (2), to be 0.45 V.

The vacuum level shifts (Δ) at the HATCN/n-ETLs junctions can be estimated from the known LUMO levels of HATCN and the ETLs and the built-in potentials at the junctions using Equation (3). They are 2.95, 1.85, and 2.35 eV for the Bphen, B3PYMPM, and TPBi layers, respectively.

$$\Delta = \mathrm{LUMO}_{\mathrm{HATCN}} - \mathrm{LUMO}_{\mathrm{ETL}} - q\psi \tag{3}$$

The vacuum level shift of 2.95 eV between the n-doped BPhen and HATCN layer is very close to the value of 2.85 eV, at the MoO_3/Mg-doped BPhen layer measured by ultraviolet and X-ray photoemission spectroscopies.[27]

All the key parameters of the materials and the devices are summarized in **Table 2**. The energy level diagrams of the HATCN/n-ETLs junctions at thermal equilibrium can be drawn from the vacuum level shifts, built-in potentials, and the depletion widths at the junctions and are displayed in **Figure 4**a–c. The downward band bending in ETLs and upward band bending in HATCN resulting from the free carrier diffusion from the n-ETL to HATCN as well as the vacuum level shifts are included in the energy level diagrams. The J–V characteristics of the CGUs are explained well using the energy level diagrams. The outstanding charge-generation efficiency in the BPhen-based device originates from the low built-in potential resulting from a high vacuum level shift, as well as the narrow depletion layer resulting from a high free carrier density in the doped BPhen layer, facilitating efficient charge injection at the interface. In other words, the charge generation in the CGUs is limited by the charge injection at the HATCN/n-ETL junctions of the generated charges at the p-HTL/HATCN junction rather than the charge generation at the junction.

Table 2. The determined interface energy alignment properties and device characteristics of CGU devices with BPhen, B3PYMPM, and TPBi.

ETLs	BPhen	B3PYMPM	TPBi
Capacitance at 0 V [nF]	23.1	7.42	5.55
Depletion layer width [nm]	5.4	16.7	22.3
Built-in potential in ETL [V]	≈0.45	≈1	≈1
Charge carrier density [cm^{-3}]	6.0×10^{18}[16]	1.39×10^{18}	0.78×10^{18}
Vacuum level shift [eV]	≈2.95	≈1.85	≈2.35
Forward voltage at 10 mA cm^{-2} [V]	0.39	1.35	1.88
Reverse voltage at –10 mA cm^{-2} [V]	–0.56	–2.9	–3.07
$\lvert V_{Rev} + V_{For} \rvert$ at ±10 mA cm^{-2} [V]	0.17	1.55	1.19

The mechanism of charge carrier generation is quite similar to the tunneling process in the p-HTL/n-ETL heterojunction.[28] However, there is a subtle difference between them: in the case of p-HTL/n-ETL CGU, the electron tunneling occurs from the highest occupied molecular orbital (HOMO) of p-HTL to the LUMO of n-ETL, which is the rate-limiting step of the charge-generation process, but in the CGUs consisting of p-HTL/HATCN/n-ETLs, charge carriers are easily generated at the junction of the HTL and HATCN, then the electron tunneling occurs from the LUMO of HATCN to the LUMO of n-ETL (n–n junction), which is the rate-limiting step of the charge-generation process. The difference in the charge generation in the devices are schematically illustrated in Figure 4d,e for the p-HTL/HATCN/n-ETLs and p-HTL/n-ETLs CGUs. The tunneling in the n–n junction can be very easy due to low barrier height compared to the tunnelling in the p–n junction if we consider the low doping efficiency in organic semiconductors.[16,29–31] One example is shown in **Figure 5** where the J–V characteristics of the n-BPhen CGU are compared with the ITO/*p*-*N*,*N*′-diphenyl-*N*,*N*′-bis (3-methylphenyl)-[1,1′-biphenyl]-4,4′-diamine (MeO-TPD) (8 wt% doped with ReO_3, 15 nm)/n-BPhen (15 wt% doped with Rb_2CO_3, 30 nm)/Al CGU, which is one of the most efficient p-HTL/n-ETL CGUs. The figure clearly shows orders of magnitude difference in the generated current at same voltages.

3. Conclusions

In summary, we have systematically studied the rate-limiting step of charge generation in CGUs composed of p-HTL/HATCN as a deep-lying LUMO material/n-ETL, where TAPC was used

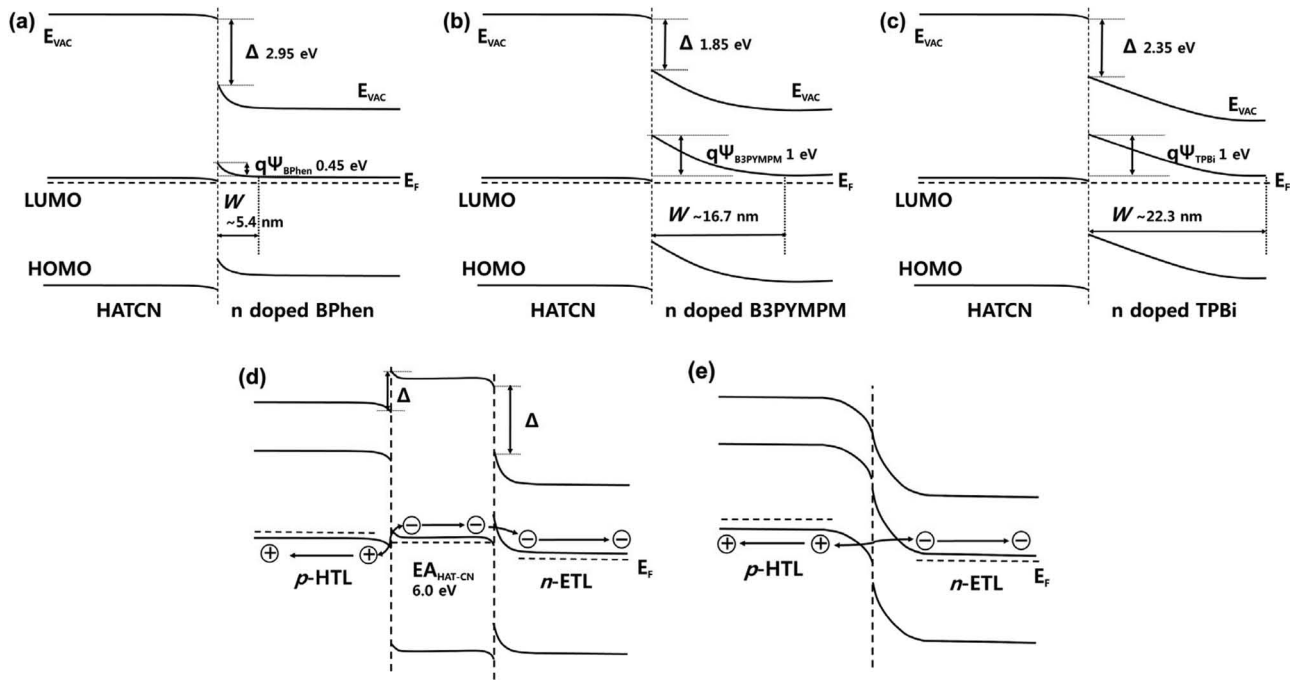

Figure 4. Energy level alignment diagrams of the HATCN/Rb_2CO_3-doped ETLs at thermal equilibrium, with the condition determined by *C–V* measurements: a) BPhen, b) B3PYMPM, and c) TPBi. The schematic energy level alignment diagrams of d) p-TAPC/HATCN/n-BPhen CGU and e) p-HTL/n-ETL CGU.

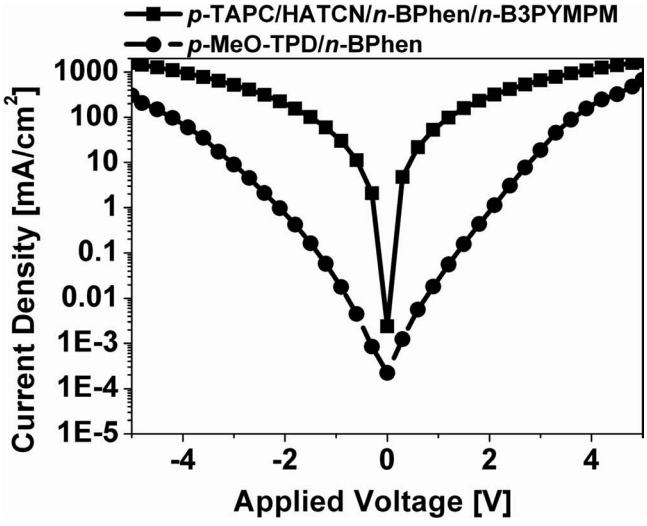

Figure 5. The *J–V* characteristics of the ITO/p-TAPC/HATCN/n-BPhen/n-B3PYMPM/Al charge generation unit (filled rectangles) and the ITO/p-MeO-TPD (8 wt% doped with ReO_3, 15 nm)/n-BPhen (15 wt% doped with Rb_2CO_3, 30 nm)/Al charge generation unit (filled circles).

as the HTL and BPhen, B3PYMPM, and TPBi were used as the ETLs. Vacuum level shifts, depletion widths, and built-in potentials were estimated using the *C–V* measurements to get the energy level alignment at the HATCN/n-ETL junction. The energy level alignment determined by the *C–V* measurements and the *J–V* characteristics of the structure clearly showed that the electron injection at the HATCN/n-ETL junction limits the charge generation in the CGUs rather than charge generation itself at the p-HTL/HATCN junction. Therefore the charge carrier generation in the CGUs depends on the vacuum level shift at the HATCN/n-ETL and the free carrier density of an ETL rather than the LUMO energy level of the ETL. The *J–V* and *C–V* characteristics revealed that the most efficient n-ETL was BPhen among BPhen, B3PYMPM, and TPBi. Consequently, the CGU with 30 mol% Rb_2CO_3-doped BPhen formed with the HATCN layer generates charges very efficiently, and the excess voltage required to generate the current density of ±10 mA cm^{-2} was around 0.17 V, which is extremely small compared with the literature values reported to date.

4. Experimental Section

Fabriation of the Devices with the CGUs: The devices with the CGUs were fabricated by thermal evaporation onto cleaned glass substrates precoated with 150-nm-thick ITO without vacuum breaking. Prior to organic layer deposition, the ITO substrates were cleaned with ultrapurified water, acetone, and isopropyl alcohol and then dried in an oven at 80 °C. Precleaned ITO substrates were exposed to ambient UV-ozone for 10 min. All layers were grown by thermal evaporation at a base pressure of $<5 \times 10^{-7}$ Torr. Layers were deposited in the following order: 8 wt% ReO_3-doped TAPC (30 nm)/HATCN (20 nm)/n-doped ETLs (20 nm)/15 wt% Rb_2CO_3-doped B3PYMPM (30 nm)/Al (100 nm). BPhen, B3PYMPM, and TPBi were selected as ETLs. Rb_2CO_3 was used as the n-dopant with a 30 mol% concentration in the devices. The devices were encapsulated immediately after organic and metal deposition under a nitrogen atmosphere using an epoxy glue and cavity glass lids. The active area of each device was 2 mm × 2 mm.

J–V and C–V Measurements: The *J–V* characteristics of the devices were measured using a Keithley 237 semiconductor parameter analyzer and *C–V* measurements were performed using an impedance analyzer

(Solartron 1287) at a constant frequency of 1 kHz with a time delay of 5 s between the data points and an applied ac bias voltage of 10 mV.

Acknowledgements

This work was supported by the industrial strategic technology development program (10035225, development of core technology for high performance AMOLED on plastic) funded by MKE/KEIT.

Received: September 17, 2011
Revised: November 10, 2011
Published online: December 16, 2011

[1] T. Matsumoto, T. Nakada, J. Endo, K. Mori, N. Kawamura, A. Yokoi, J. Kido, *SID Digest* **2003**, *34*, 979.
[2] L. S. Liao, K. P. Klubek, C. W. Tang, *Appl. Phys. Lett.* **2004**, *84*, 167.
[3] H. Kanno, R. J. Holmes, Y. Sun, S. Kena-Cohen, S. R. Forrest, *Adv. Mater.* **2006**, *18*, 339.
[4] M.-Y. Chan, S.-L. Lai, K.-M. Lau, M.-K. Fung, C.-S. Lee, S.-T. Lee, *Adv. Funct. Mater.* **2007**, *17*, 2509.
[5] L.-S. Liao, W. K. Slusarek, T. K. Hatwar, M. L. Ricks, D. L. Comfort, *Adv. Mater.* **2008**, *20*, 324.
[6] L. S. Liao, K. Pl Klubek, *Appl. Phys. Lett.* **2008**, *92*, 223311.
[7] S. Hamwi, J. Meyer, M. Kroger, T. Winkler, M. Witte, T. Riedl, A. Kahn, W. Kowalsky, *Adv. Funct. Mater.* **2010**, *20*, 1762.
[8] M. Terai, T. Tsutsui, *Appl. Phys. Lett.* **2007**, *90*, 083502.
[9] D.-S. Leem, J.-H. Lee, J.-J. Kim, J.-W. Kang, *Appl. Phys. Lett.* **2008**, *93*, 103304.
[10] M. K. Fung, K. M. Lau, S. L. Lai, C. W. Law, M. Y. Chan, C. S. Lee, S. T. Lee, *J. Appl. Phys.* **2008**, *104*, 034509.
[11] C. W. Law, K. M. Lau, M. K. Fung, M. Y. Chan, F. L. Wong, C. S. Lee, S. T. Lee, *Appl. Phys. Lett.* **2006**, *89*, 133511.
[12] K. S. Yook, S. O. Jeon, S.-Y. Min, J. Y. Lee, H.-J. Yang, T. Noh, S.-K. Kang, T.-W. Lee, *Adv. Funct. Mater.* **2010**, *20*, 1797.
[13] C.-W. Chen, Y.-J. Lu, C.-C. Wu, E. H.-E. Wu, C.-W. Chu, Y. Yang, *Appl. Phys. Lett.* **2005**, *87*, 241121.
[14] T.-W. Lee, T. Noh, B.-K. Choi, M.-S. Kim, D. W. Shin, J. Kido, *Appl. Phys. Lett.* **2008**, *92*, 043301.
[15] Y.-K. Kim, J. W. Kim, Y. Park, *Appl. Phys. Lett.* **2009**, *94*, 063305.
[16] a) J.-H. Lee, P.-S. Wang, H.-D. Park, C.-I. Wu, J.-J. Kim, *Org. Electron.* **2011**, *12*, 1763; b) J.-H. Lee, D.-S. Leem, H.-J. Kim, J.-J. Kim, *Appl. Phys. Lett.* **2009**, *94*, 123306.
[17] S. Naka, H. Okada, H. Onnagawa, T. Tsutsui, *Appl. Phys. Lett.* **2000**, *76*, 197.
[18] H. Sasabe, D. Tanaka, D. Yokoyama, T. Chiba, Y.-J. Pu, K.-i. Nakayama, M. Yokoyama, J. Kido, *Adv. Funct. Mater.* **2011**, *21*, 336.
[19] W.-Y. Hung, T.-H. Ke, Y.-T. Lin, C.-C. Wu, T.-H. Hung, T.-C. Chao, K.-T. Wong, C.-I. Wu, *Appl. Phys. Lett.* **2006**, *88*, 064102.
[20] J. R. Gallegosa, A. H. Francisa, N. W. Ockwiga, P. G. Rasmussena, R. G. Raptis, P. R. Challenc, I. Ouedraogo, *Synth. Met.* **2009**, *159*, 1667.
[21] K. Harada, A. G. Werner, M. Pfeiffer, C. J. Bloom, C. M. Elliott, K. Leo, *Phys. Rev. Lett.* **2005**, *94*, 036601.
[22] H. Kleemann, R. Gutierrez, F. Lindner, S. Avdoshenko, P. D. Manrique, B. Lussem, G. Cuniberti, K. Leo, *Nano Lett.* **2010**, *10*, 4929.
[23] R. L. Anderson, *Solid-State Electon.* **1962**, *5*, 341.
[24] S. M. Sze, K. K. NG, *Physics of Semiconductor Devices*, 3rd ed. Wiley-Interscience, Hoboken, NJ **2007**, Ch. 3.
[25] M. Meier, S. Karg, W. Riess, *J. Appl. Phys.* **1997**, *82*, 1961.
[26] A. P. Marchetti, K. E. Sassin, R. H. Young, L. J. Rothberg, D. Y. Kondakov, *J. Appl. Phys.* **2011**, *109*, 013709.
[27] Q. Y. Bao, J. P. Yang, Y. Q. Li, J. X. Tang, *Appl. Phys. Lett.* **2010**, *97*, 063303.
[28] M. Kroger, S. Hamwi, J. Meyer, T. Dobbertin, T. Riedl, W. Kowalsky, H.-H. Jonannes, *Phys. Rev. B* **2007**, *75*, 235321.
[29] J.-H. Lee, D.-S. Leem, J.-J. Kim, *Org. Electron.* **2010**, *11*, 486.
[30] J.-H. Lee, H.-M. Kim, K.-B. Kim, J.-J. Kim, *Org. Electron.* **2011**, *12*, 950.
[31] J.-H. Lee, H.-M. Kim, K.-B. Kim, R. Kabe, P. Anzenbacher Jr., J.-J. Kim, *Appl. Phys. Lett.* **2011**, *98*, 173303.